

The 8-Hydroxyquinolinium Cation as a Lead Structure for Efficient Color-Tunable Ionic Small Molecule Emitting Materials

Brando Adranno, Olivier Renier, Guillaume Bousrez, Veronica Paterlini, Glib V. Baryshnikov, Volodymyr Smetana, Shi Tang, Hans Ågren, Andreas Metlen, Ludvig Edman, Anja-Verena Mudring,* and Robin D. Rogers


Albeit tris(8-hydroxyquinolinato) aluminum (Alq_3) and its derivatives are prominent emitter materials for organic lighting devices, and the optical transitions occur among ligand-centered states, the use of metal-free 8-hydroxyquinoline is impractical as it suffers from strong nonradiative quenching, mainly through fast proton transfer. Herein, it is shown that the problem of rapid proton exchange and vibration quenching of light emission can be overcome not only by complexation, but also by organization of the 8-hydroxyquinolinium cations into a solid rigid network with appropriate counter-anions (here bis(trifluoromethanesulfonyl)imide). The resulting structure is stiffened by secondary bonding interactions such as π -stacking and hydrogen bonds, which efficiently block rapid proton transfer quenching and reduce vibrational deactivation. Additionally, the optical properties are tuned through methyl substitution from deep blue (455 nm) to blue-green (488 nm). Time-dependent density functional theory (TDFT) calculations reveal the emission to occur from which an unexpectedly long-lived S_1 level, unusual for organic fluorophores. All compounds show comparable, even superior photoluminescence compared to Alq_3 and related materials, both as solids and thin films with quantum yields (QYs) up to 40–50%. In addition, all compounds show appreciable thermal stability with decomposition temperatures above 310 °C.

1. Introduction

Global energy consumption is continuously rising. Electricity usage, of which 15% is due to lighting,^[1] is expected to increase to 21% of the global energy consumption by 2030.^[2] Therefore, the development of energy-efficient and environmentally benign light sources such as organic light-emitting diodes (OLEDs)^[3] and light-emitting electrochemical cells (LECs) is of utmost importance.^[4] The latter technology is receiving increasing attention from the scientific community because of its simple device structure which reduces the number of materials and components and allows for simple and efficient manufacturing.^[5] While OLEDs commonly feature an air- and thickness-sensitive multilayer structure that often requires fabrication by expensive thermal vacuum evaporation, LECs can be fabricated in an air-stable and robust three-layer structure (an active material sandwiched between two electrodes) by cost-efficient solution-processing, such as coating and

B. Adranno, O. Renier, G. Bousrez, V. Paterlini, V. Smetana, A.-V. Mudring, R. D. Rogers
Department of Materials and Environmental Chemistry
Stockholm University
Svante Arrhenius väg 16C, SE-10691 Stockholm, Sweden
E-mail: anja-verena.mudring@mmk.su.se

G. V. Baryshnikov
Department of Science and Technology
Laboratory of Organic Electronics
Linköping University
SE-60174 Norrköping, Sweden

 The ORCID identification number(s) for the author(s) of this article can be found under <https://doi.org/10.1002/adpr.202200279>.

© 2023 The Authors. Advanced Photonics Research published by Wiley-VCH GmbH. This is an open access article under the terms of the Creative Commons Attribution License, which permits use, distribution and reproduction in any medium, provided the original work is properly cited.

DOI: 10.1002/adpr.202200279

S. Tang, L. Edman
The Organic Photonics and Electronics Group
Umeå University
SE-90187 Umeå, Sweden

H. Ågren
Department of Physics and Astronomy
Uppsala University
Box 516, SE-751 20 Uppsala, Sweden

A. Metlen, R. D. Rogers
The QUILL Research Centre and School of Chemistry and Chemical Engineering
The Queen's University of Belfast
Belfast, Northern Ireland BT9 5AG, UK

A.-V. Mudring
Intelligent Advanced Materials (iAM)
Department of Biological and Chemical Engineering and iNANO
Aarhus University
8000 Aarhus C, Denmark

printing. As active materials, emissive ionic liquids (ILs) serve as a promising class of materials, because they have the potential to combine ionic as well as electronic conductivity with electroluminescence.^[6]

However, one of the strongest current challenges for their commercialization is the operational lifetime. The current state of the art is a few thousand hours for a yellow-emitting LEC.^[7] The stability is even lower for blue LECs, because of the higher required drive voltage which can lead to the destruction of the material,^[8] amongst other factors. It is often the emitter that degrades during LEC operation, and recent efforts have therefore aimed at developing improved emitter materials like ionic transition metal complexes (iTMCs),^[9] quantum dots (QDs),^[10] and small molecules (SMs).^[11] SMs are particularly interesting as they can be all-organic and thereby omit the use of critical or toxic transition metals. SMs can be either neutral,^[12] thereby requiring the addition of an electrolyte, or ionic which technically would avoid the use of an additional electrolyte.^[13] Ionic SMs have been utilized as emitters in LEC devices that deliver external quantum yields (EQYs) of close to 13%.^[14] The development of SMs is typically based on the identification of a lead structure that can easily be functionalized for color tuning, and recent LECs based on SMs have demonstrated promising performance, particularly for blue light emission.^[15] Most SMs feature extensively aromatic systems that can be susceptible to self-quenching,^[15] which, however, can be suppressed by functionalization with long alkyl spacers for spatial separation of the emitting centers.^[13,16] However, such compounds often require a complex, rather materials-intensive multistep synthesis, which makes their production challenging and reduces the greenness of the LEC. Galvanized by the challenge of finding more environmentally benign and economically accessible alternatives without compromising the luminescence performance, we hypothesize that the extremely compact organic SM series of 8-hydroxyquinolines (8Hqs) can satisfy these requirements and be a suitable platform for new emitter materials. Neutral 8Hqs derivatives are well known as efficient emitter materials in OLEDs.^[17] In particular, major attention has been directed toward the yellow-green emitting (550 nm) complex tris(8-hydroxyquinolato) aluminum (Alq₃), which was first reported in 1987.^[18] The photophysical properties of neutral 8Hq and its derivatives have been extensively explored over the past few decades. It was found that the emission wavelength of the 8Hq can easily be tuned through the functionalization with both electron-donating and electron-withdrawing groups.^[19] Since then, it has been confirmed that both the highest occupied molecular orbital (HOMO) and the lowest unoccupied molecular orbital (LUMO) levels of Alq₃, which are responsible for the light emission, are located on the organic ligand, i.e., the deprotonated 8-hydroxyquinoline.^[20] Unfortunately, 8Hq itself shows a very weak photoluminescence quantum yield (PLQY), which is attributed to a fast proton transfer.^[21] The lifetime and PLQY of the free unsubstituted 8Hq are much lower in solution than in the solid state as a result of the proton-exchange quenching.^[22] This proton transfer is observed

also for its cationic and anionic forms, albeit in strong acids and bases a higher PLQY is observed, which has been attributed to reduced proton transfer dynamics.^[21b,23] Likewise, in complexes, like Alq₃, this proton transfer is inhibited and therefore they show quite high PLQY and can so find application in electroluminescent devices.^[19,20] Interestingly, a few ionic SMs featuring 8-hydroxyquinolinium [8HqH]⁺ as the cation, such as the succinate or squarate, have been reported to feature blue light emission.^[24] This encouraged us to further investigate salts of [8HqH]⁺ and explore the possibility to suppress the proton transfer by strong hydrogen bonds. Our hypothesis is that the formation of a rigid hydrogen-bonded network will hinder the proton transfer and thereby increase the efficiency for a radiative deactivation of the excited state. We selected bis(trifluoromethanesulfonyl)imide ([Tf₂N][−]) as the counter-anion, since it offers multiple hydrogen-bonding acceptor sites, because it has been demonstrated to be compatible with a number of different cations, and since it is reported to be more (chemically) stable in LEC devices than other fluorine-based anions, like [PF₆][−] and [BF₄][−].^[25] We have tested our hypothesis by a systematic investigation of: 1) 8-hydroxyquinolinium bis(trifluoromethanesulfonyl)imide [8HqH][Tf₂N], and its two methyl-derivatives, 2) 5-methyl-8-hydroxyquinolinium bis(trifluoromethanesulfonyl)imide [5Me8HqH][Tf₂N], and 3) 2-methyl-8-hydroxyquinolinium bis(trifluoromethanesulfonyl)imide [2Me8HqH][Tf₂N].

It has been demonstrated that the HOMO and LUMO of 8-hydroxyquinolines are mainly located on the phenolic ring and the pyridinium ring, respectively.^[20] Electron-donating methylation in different positions of the 8-hydroxyquinoline will therefore either affect the energy of the HOMO and the LUMO. For instance, the methylation of the phenolic ring system will increase the HOMO and result in a smaller bandgap and lower energy emission. In contrast, the methylation of the pyridinium ring system will increase the LUMO and result in a larger bandgap and higher energy emission.

2. Results and Discussion

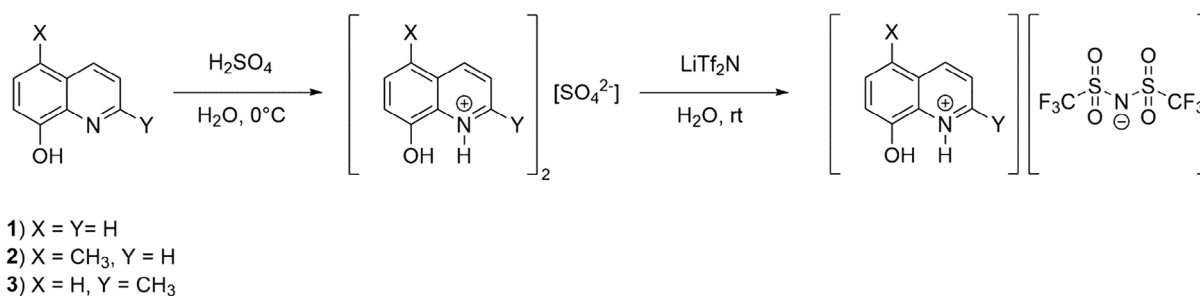
2.1. Synthesis

[8HqH][Tf₂N] (1), [5Me8HqH][Tf₂N] (2), and [2Me8HqH][Tf₂N] (3) could be obtained in high yields in a facile two-step synthesis from the respective 8-hydroxyquinoline by initial protonation with sulfuric acid (H₂SO₄, 98%) and subsequent metathesis with lithium bis(trifluoromethanesulfonyl)imide (LiTf₂N) in water (Scheme 1).

2.2. Crystal Structures

Isothermal evaporation of aqueous solutions of 1–3 at room temperature yielded crystals of sufficient quality for single-crystal X-ray diffraction (SCXRD) studies. The asymmetric unit for each compound is composed of one cation charge-balanced by one [Tf₂N][−] anion (Figure S1, Supporting Information). Upon protonation of 8-hydroxyquinoline and its methyl-derivatives an increase of the internal C–N(H)–C angle occurs from 118.05(1)° for the neutral form^[26] to 123.0(3)° for 1, 120.0(1)° for 2, and 124.0(2)° for 3. The counter-anion, [Tf₂N][−], adopts

R. D. Rogers
Department of Chemistry & Biochemistry
The University of Alabama
Tuscaloosa, AL 35487, USA



Scheme 1. Synthesis of: compound [8HqH][Tf₂N] (**1**), [5Me8HqH][Tf₂N] (**2**), and [2Me8HqH][Tf₂N] (**3**).

a *cis* conformation in all three structures, with a slight deviation in the torsion angle between the -CF₃ group and the sulfur atoms of: 1) $\angle = 26.6(2)^\circ$, 2) $\angle = 18.7(2)^\circ$, 3) $\angle = 23.0(2)^\circ$. The *cis* conformation is thermodynamically less stable than the *trans* conformation in the gas phase.^[27] However, directional interactions and packing effects can alter the situation in the solid state, with hydrogen bonding having an important role, especially since 8-hydroxyquinolines have demonstrated a predisposition for extended hydrogen-bonded networks.^[28] In each structure, moderate^[29] hydrogen bonds between each cation and two anions and vice versa are observed. In all three compounds, the strongest interactions (**Table 1**, **Figure 1**) occur between the protonated nitrogen and phenolic oxygen and the oxygen atoms of the -SO₂ groups in the [Tf₂N]⁻ anions. In the crystal structure of **1**, those hydrogen bonds occur only to one and not both sulfonyl groups of an anion, yielding an extended hydrogen-bonded helix of alternating cations and anions (**Figure 1a**). That helix is associated with the 2₁ axis and is somewhat squashed with the major radii of 9.743(2) and 3.686(2) Å and the pitch of 8.770(2) Å. Methyl substitution prevents the formation of such an arrangement in **2** and **3**, and rather forms two ion pairs (**Figure 1b,c**, S3,S4, Supporting Information), although with significant differences. In **3**, the two cations in the dimer are nearly coplanar with the bridging anions perpendicular to (above and below) this plane. In **2**, the cations are parallel but offset by ≈ 2.6 Å with the anions perpendicular to these planes and mostly residing between them.

In all compounds, the positive-charge-rich pyridine N participates in charge-assisted hydrogen bonding to an anion, in an ionic interaction to an anion on the opposite side from the π -stacking, and in π -stacking to the phenolic region of an adjacent cation. The three compounds not only differ in hydrogen

bonding but have different π -stacking motifs which are complementing the ionic interactions between the -SO₂ groups of the anions and the charge-rich N of the cations.

The hydrogen-bonded helices of **1** feature continuous 1D π - π motifs with each pyridine directly above the phenolic moiety of a neighboring cation ($d_{\text{N-Cg}} = 3.463(2)$ Å) and the -SO₂ group of an anion above but offset ($d_{\text{N-O}} = 3.000(4)$ Å). This places the most electron-rich portions of the cation and the anion in close proximity to the electron-poor pyridine N atom. The adjacent cations are nearly parallel but flipped and rotated relative to each other by $\approx 120^\circ$. The direction of the rotation alternates between clock- and anticlockwise with each next cation. **2** also exhibits continuous 1D π - π motifs with essentially the same stacking features. The hydrogen-bonded rectangles (**Figure 1b**) stack with each pyridine directly above the phenolic moiety of a neighboring dimer ($d_{\text{N-Cg}} = 3.57(1)$ Å) with the -SO₂ group ($d_{\text{N-O}} = 3.15(2)$ Å) of another dimer directly above. The nearly parallel cations are flipped and rotated relative to each other by $\approx 110^\circ$ in a similar manner to **1**. Compound **3** has the electron-donating methyl group directly positioned on the pyridine ring, which reduces the overall positive charge on the N atom and which is reflected in the unique packing exhibited by **3** compared with **1** and **2**. **3** exhibits the shortest cation-anion contacts, revealing higher rigidity of the environment surrounding the cationic moiety. This is at least partially a result of the discontinuous π -stacking found in **3** compared with **1** and **2**. In **3**, the hydrogen-bonded dimers align such that the cations stack pyridine to the phenolic moiety by a simple rotation of 180° . In this case, the pyridine ring C3-C4 stacks above the phenolic moiety ($d_{\text{C-Cg}} = 3.538(4)$ and $3.640(4)$ Å) and the -SO₂ group ($d_{\text{N-O}} = 3.082(4)$ Å) between the two cations. This dimeric form of the cation stacking leads to a modified anionic environment in the form of parallel six-membered rings surrounding each pair of cations.

Despite having distinct local features, the molecular packing in the crystal structures of **1–3** is quite similar (**Figure S5–S7**, Supporting Information). The most distinct features include checkered cationic-anionic salt-like motifs in all structures and clear segregation of the charged hydrophilic parts and uncharged, F-containing parts. The latter is particularly obvious in the crystal structures of **2** and **3** with distinct layers formed by -CF₃ groups. Such segregation has not been observed in **1** due to different mutual orientations of the [Tf₂N]⁻ anions but is still present in the form of chains. Although no significant CH...F interactions are present in any structure -CF₃ groups are always oriented maximally away from the N-H and O-H cationic

Table 1. The strongest hydrogen bonds in the crystal structures of **1–3**.

	D-H...A ^{a)}	<i>d</i> (D-H), [Å]	<i>d</i> (H...A), [Å]	<i>d</i> (D...A), [Å]	\angle (D-H...A), [°]
1	N-H...O	0.86(3)	2.104(3)	2.870(4)	148.2(2)
	O-H...N	0.82(3)	2.116(3)	2.893(4)	158.2(2)
2	N-H...O	0.86(1)	2.03(2)	2.74(2)	140.3(9)
	O-H...O	0.98(1)	1.72(1)	2.69(2)	172.4(9)
3	N-H...O	0.85(4)	2.12(4)	2.945(3)	164.1(4)
	O-H...O	0.84(5)	1.92(5)	2.742(4)	166.6(4)

^{a)}D = Donor, A = Acceptor.

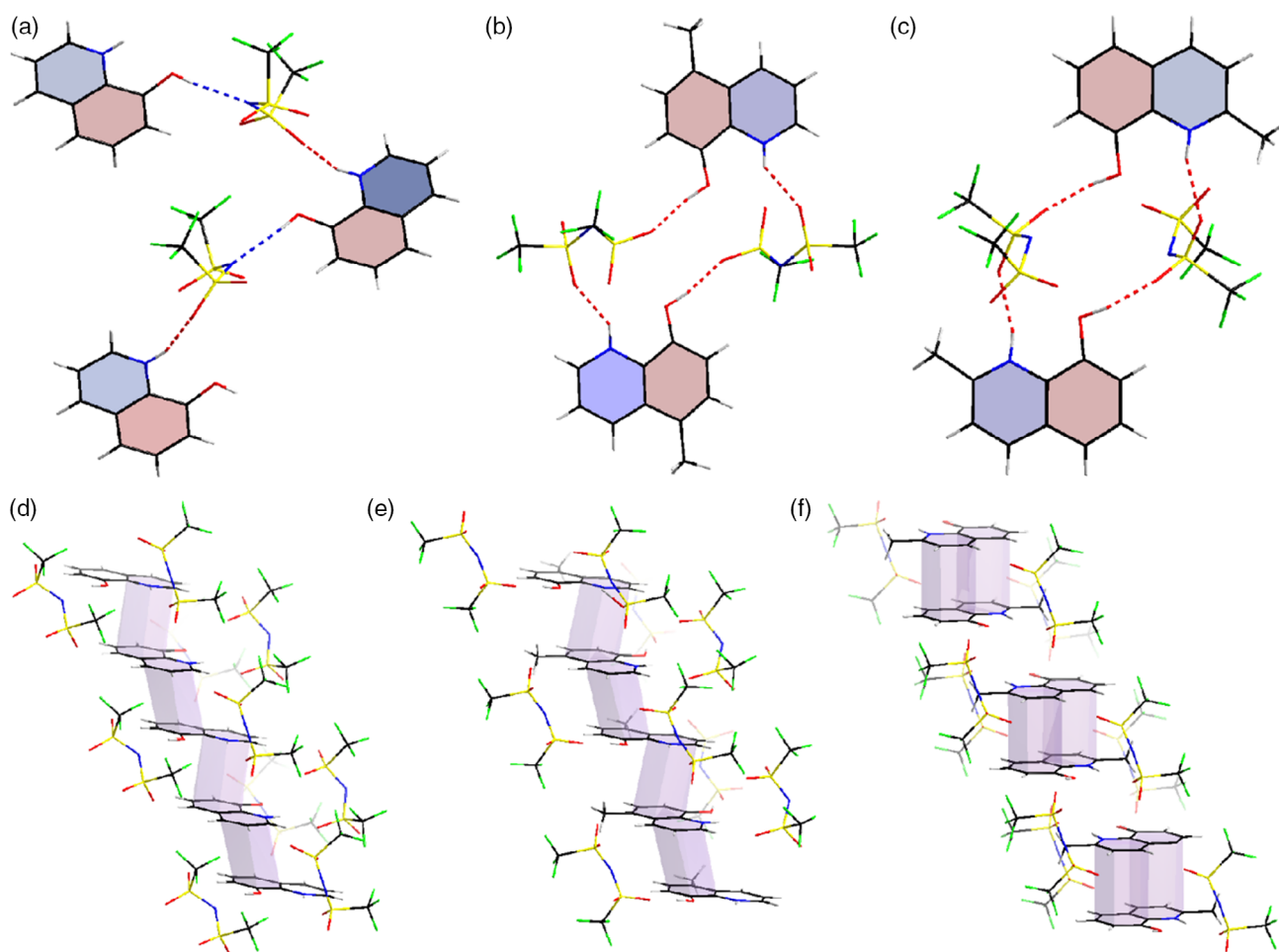


Figure 1. Representation of the strongest hydrogen bond connectivities in: a) **1**, b) **2**, and c) **3**. Stair: d) **1** and e) **2** and f) **3** dimeric head-to-tail π -stacking.

groups but towards each other. This bonding and geometric optimization may serve as a justification for the thermodynamically less stable *cis* conformation of the $[\text{Tf}_2\text{N}]^-$ anions observed in all structures. In summary, the form of the alignment differs from helical to parallel, which is reflected in the connectivity within the cationic motifs. There are three unique packing arrangements (Figure 1), which show the flexibility of packing with these three interactions. The cationic chains in **1–2** are uniform and continuous leading to the helical alignment of the anionic chain around, while the pair-wise distribution of the bonding schemes in **3** leads to the segregation and parallel alignment of the six-membered anionic rings. Thus, with respect to packing motifs, **2** shares helix-like π -stacking motifs with **1** (c.f. Figure 1d,e) and association of a cation with two anions with **3** (Figure 1b,c). The supramolecular packing of the three compounds is primarily a result of π -stacking, hydrogen bonding, and ionic interactions between the anions and the charge-rich N of the pyridine moiety. The packing of the ions in the structures creates an unsuitable environment for fast proton transfer, therefore mitigating radiationless deactivation of the excited state. More details will be provided below when discussing the photophysical properties of the materials. Furthermore, the alignment of the anions leads to the segregation of the charged hydrogen bonded parts

and uncharged $-\text{CF}_3$ groups (Figure S5–S7, Supporting Information) that could have further implications for the miscibility with other electrolytes and film production.

2.3. Thermal Behavior

Thermogravimetric analysis (TGA) of **1–3** reveals a good thermal stability for all three compounds (Table 2, Figure S23–S25, Supporting Information), with the onset (5% material loss) of

Table 2. Thermal properties of **1–3**. The temperatures of the decomposition steps are reported with the percentage of mass loss in brackets.

	1st Decomposition Step [°C] ^{a)}	2nd Decomposition Step [°C] ^{a)}	T_{melt} [°C] ^{b)}	T_{cryst} [°C] ^{b)}	$\Delta T_{\text{supercooling}}$ [°C]
1	311 (87%)	– ^{c)}	112	60	52
2	323 (74%)	459 (20%)	91	85	6
3	320 (74%)	457 (20%)	127	94	33

^{a)}These values correspond to the $T_{5\% \text{onset}}$ mass loss. ^{b)}These values correspond to the onset of the transition. ^{c)}ill-defined.

thermal decomposition ($T_{5\% \text{ onset}}$) at: 287 °C (1), 293 °C (2), and 310 °C (3) (mass loss of $\approx 87\%$ for 1 and $\approx 74\%$ for 2 and 3). The methyl-substituted compounds, 2 and 3, exhibit a second decomposition step, corresponding to $\approx 20\%$ mass loss, at: 414 °C (2) and 431 °C (3), while 1 is characterized by a less defined final mass loss.

The onsets of the melting points of 1–3 (Table 2, Figure S26–S28, Supporting Information) determined by differential scanning calorimetry (DSC) range from 91 °C (2) to 127 °C (3). The higher melting point of 3 can be rationalized by a combination of strong cation–anion interaction, by significant hydrogen bonds between the anions and cations, and by dimeric π -stacking configuration (vide supra). This leads to an overall stiffer structure, which would need most likely more energy to break and therefore achieve a liquid state. 2 shows the weakest bonding interactions, and, consequently, has the lowest melting point. In contrast to 2, 1 and 3 exhibit strong supercooling even at a slow cooling rate of 1 °C min^{-1} of $\Delta T_{\text{supercooling}} = 52\text{ °C}$ and 33 °C , respectively. Strong supercooling or hindered crystallization are common for ILs,^[30] albeit only 2 (barely) fits the formal definition of an IL with a melting temperature below 100 °C. In the context of the fabrication of electroluminescent devices, this supercooling effect could be exploited for thin-film deposition of the supercooled and molten material at a reasonable temperature by solvent-free coating or printing.

2.4. Photophysical Properties

The optical properties of 1–3 were investigated in both the solid phase and in a $2 \times 10^{-4}\text{ M}$ aqueous solution. The UV–vis absorption spectra of the grounded powdered samples (Figure 2, black lines) show one intense transition near 250 nm and a broader and weaker one between 300 and 400 nm, corresponding to π – π^* transitions in the cations as also observed for 8-hydroxyquinoline.^[31] The additional tail between 400 and 600 nm is assigned to aggregation effects, similar to what has been observed for other compounds with significant π – π interactions such as sodium salicylate^[32] and others.^[33] Compounds 1 and 2 absorb relatively stronger at lower energy than 3, because of their more extended π -stacking in the stair configuration.

The assignment of the low-energy absorption bands to aggregation effects is confirmed by absorption measurements of the compounds in $2 \times 10^{-4}\text{ M}$ aqueous solutions (Figure 2, red lines), where those bands are not observed. In addition, the π – π^* transitions are blue-shifted due to a negative solvatochromic effect of water which raises the LUMO (vide infra, Section 2.5). The optical bandgaps ΔE_g , determined as $1240/\lambda_{\text{onset}}$, are 3.06 eV (405 nm) for 1, 2.84 eV (437 nm) for 2, and 3.12 eV (397 nm) for 3.

The excitation spectra of powder samples 1–3, recorded at: $\lambda_{\text{em}} = 460\text{ nm}$ (1), 488 nm (2), and 455 nm (3), revealed weak transitions in the 300–400 nm region with maxima at: 400 nm (1), 420 nm (2), and 393 nm (3) in agreement with the absorption spectra (Figure 3, blue lines). The major differences in the absorption spectra are the absence of transitions at low energies from 400 to 600 nm corresponding to π – π interactions in the solid since they do not contribute to the main emission peaks at which the spectra were monitored.

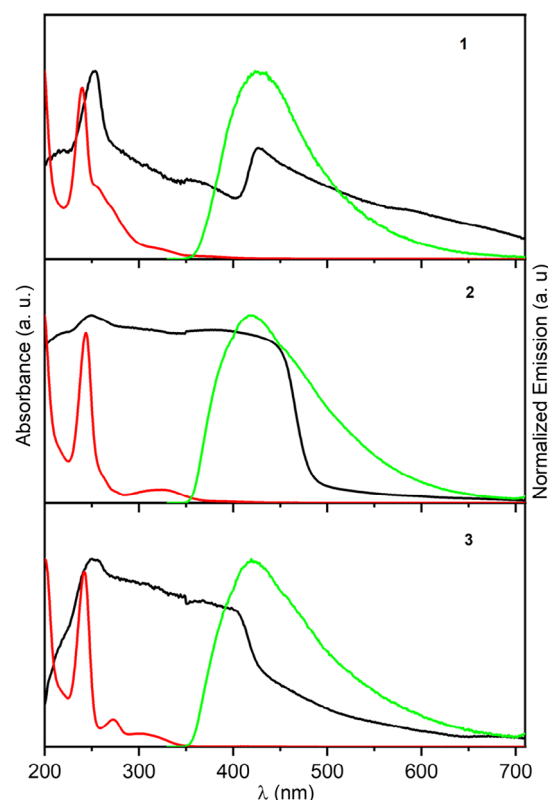


Figure 2. Normalized UV–vis absorption spectra of 1–3 as powders (black lines) and in dilute $2 \times 10^{-4}\text{ M}$ aqueous solutions (red lines), and their emission spectra in the aqueous solutions (green lines, $\lambda_{\text{ex}} = 310\text{ nm}$).

The excitation of powder 1 at 400 nm reveals a broad band emission with a maximum of 460 nm. This originates from one of the π – π transitions of the $[8\text{HqH}]^+$ moiety, similar to what has been reported for 8Hq in (acidic) solution.^[32,34] When compared with 1, the emission of the solid methylated derivatives is shifted, as expected from the perturbation of the electronic structure upon methylation, namely the methylation of the phenolic ring system will increase the HOMO level and yield a lower energy emission. In contrast, the methylation of the pyridinium ring system will increase the LUMO energy and result in a higher energy emission. Consequently, 2 shows a red shift of 28 nm after photoexcitation at 420 nm, while 3 exhibits a small blue shift of about 5 nm upon excitation at 393 nm with respect to the emission of 1.

The chromaticity coordinates, shown in a CIE 1931 diagram^[35] (Figure 4), are: 0.17 (1), 0.22; 0.24, 0.44 (2), and 0.17, 0.19 (3), which position the compounds 1 and 3 in the blue and 2 in the greenish region.

The luminescence lifetimes of all three compounds could be fitted with a monoexponential function (Equation (1)).

$$F(t) = A + B \cdot e^{-t/\tau} \quad (1)$$

The lack of a second decay component implies that these compounds do not exhibit thermally activated delayed fluorescence (TADF), which has become popular for applications in

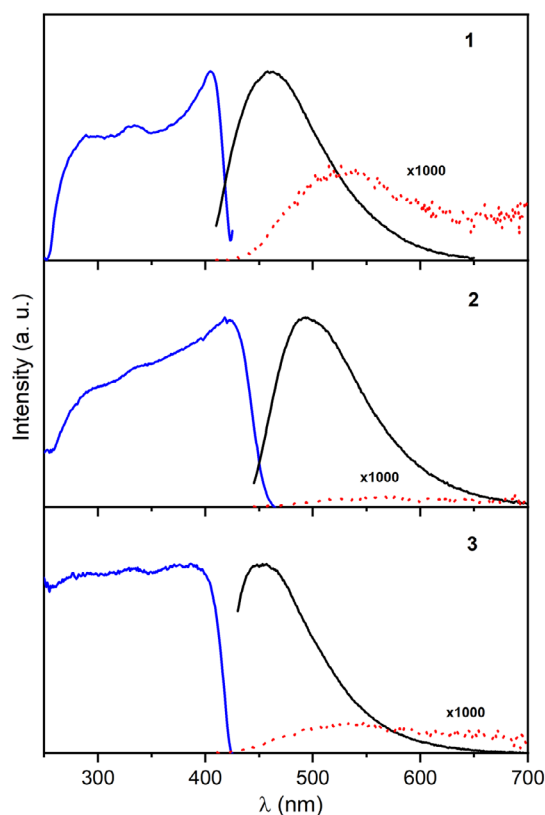


Figure 3. Excitation (blue lines, monitored at: $\lambda_{\text{em}} = 460$ nm (1), $\lambda_{\text{em}} = 488$ nm (2), and $\lambda_{\text{em}} = 455$ nm (3)) and emission (black lines, upon excitation at: $\lambda_{\text{ex}} = 400$ nm (1), $\lambda_{\text{ex}} = 420$ nm (2), $\lambda_{\text{ex}} = 393$ nm (3)) spectra of powders of 1–3 plotted with the emission spectra of the supercooled liquids (red dots, upon excitation at: $\lambda_{\text{ex}} = 400$ nm (1), $\lambda_{\text{ex}} = 420$ nm (2), $\lambda_{\text{ex}} = 393$ nm (3)), magnification of the signal by 10^3).

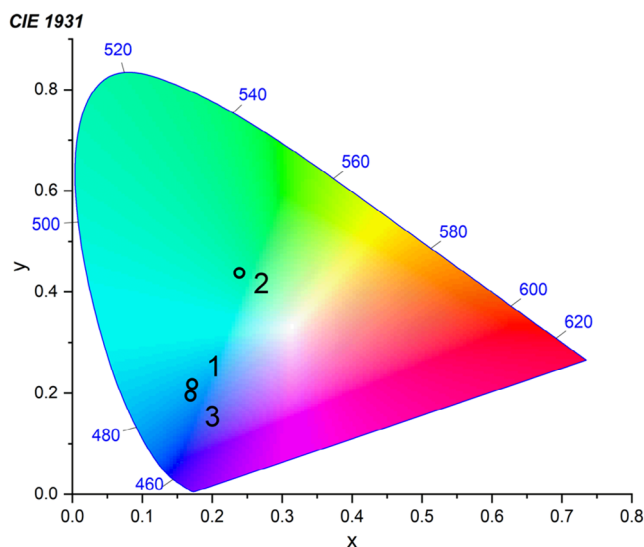


Figure 4. Color coordinates of 1–3 in the CIE 1931 diagram.

LECs.^[36] The derived lifetime of the excited state and the measured PLQY are 40 ns, 20% (1), 24 ns, 13% (2), and 47 ns, 49%

(3). The photophysical properties obtained for solid samples of 1–3 are comparable, or in some cases even better, than those reported for metal-based 8Hq materials designed for application in OLEDs. For comparison, the lifetime and the PLQY for Alq₃ powder were measured to be 19.6 ns and 32%.^[37] For the powders of the similar complex Caq₂, a lifetime of 22 ns was reported which already is quite high.^[38] Significantly shorter values were found for Zn(II) and Cd(II) complexes based on (E)-2-[(4-tert-butylphenyl)ethenyl]-8-hydroxyquinoline and (E)-2-[(2-chloro-3,4-dimethoxyphenyl)ethenyl]-8-hydroxyquinoline (11 ns).^[39]

This suggests that the favorable PL properties of 1–3 are the result of the rigid structures evoked by strong interionic forces, hydrogen bonds, and π -stacking, as identified by the structural characterization. The attainment of this rigid structure prevents the proton exchange that leads to radiationless quenching. Additionally, the stiff structure reduces rotational and vibrational motions, which strongly abate non-radiative deactivation of the excited state. To confirm this hypothesis further, and to investigate the importance of the ordered structures, emission spectra were collected for all the compounds in the amorphous supercooled state. To this end, the samples were molten in a cuvette and their properties were recorded before reaching their crystallization temperature. As expected the emission was significantly weakened and it was technically not possible to determine the radiative lifetimes and PLQY. All supercooled samples exhibit a distinct red-shift of the emission compared to the solid state of: 76 nm (1), 83 nm (2), and 92 nm (3) (Figure 3, Table 3). This points to a significant change in the local cation environment. Interestingly, the emission maxima are close to those calculated from time-dependent density functional theory (TDFT) for the isolated cations (Table 3). Likewise, it was also not possible to determine the emission lifetime and the PLQY in aqueous solutions of 1–3. The emission spectra of the aqueous solutions (Figure 3, green lines) are blue-shifted due to the solvatochromic effect of the polar solvent, and do provide important insights: the emission maximum at 410 nm can be assigned to the emission of the respective neutral 8-hydroxyquinoline species, whilst the broad shoulder in the region 420–600 nm corresponds to the protonated species. Thus, the negligibly weak fluorescence of compounds 1–3 in aqueous solution can be explained as quenching due to a process of ultrafast photoinduced proton transfer between the cations and water molecules, as previously described for 8Hq in water.^[21a]

Thin films of the three compounds spin-coated from acetonitrile solution yield similar positions for the emission maxima (442 nm for 1, 483 nm for 2, and 450 nm for 3) as observed for the crystalline solid powders (Figure S30, Supporting Information). Importantly, the PLQY of the spin-coated thin films are as high as: 44% (1), 24% (2), and 30% (3). The photophysical properties obtained for solid samples of 1–3 are comparable, or in some cases even better, than those reported for metal-based 8Hq materials designed for application in OLEDs. For comparison, thin films of the Alq₃ exhibited a PLQY of 32%.^[40] Moreover, an optical microscopy study revealed that the spin-coated material covered the substrate in a non-uniform manner, which un-continuously covered the substrate with areas of different thicknesses. These observations suggest that the compounds have crystallized also in thin films. In principle, due to the IL-nature of the compounds, solvent-free spin-coating

Table 3. Excitation and emission wavelengths measured for powder samples, supercooled liquids, and aqueous solutions (2×10^{-4} M) of 1–3 collected at room temperature together with lifetimes, photoluminescence quantum yield, optical bandgap (ΔE_{λ} for the powder samples), and values calculated with time-dependent density functional theory (TDFT).

		λ_{ex} [nm]	λ_{em} [nm]	τ [ns]	PLQY	ΔE_{λ} [eV, nm]
1	Powder	400	460	40	20%	3.1 405
	Supercooled	400	526	– ^{a),b)}	–	–
	H ₂ O	310	431	–	–	–
	TDFT ^{c)}	–	523 (2.37 eV)	–	–	3.0 413
2	Powder	420	488	24	13%	2.8 437
	Supercooled	420	571	–	–	–
	H ₂ O	310	420	–	–	–
	TDFT ^{c)}	–	589 (2.10 eV)	–	–	2.8 443
3	Powder	393	455	47	49%	3.1 397
	Supercooled	393	547	–	–	–
	H ₂ O	310	419	–	–	–
	TDFT ^{c)}	–	508 (2.44 eV)	–	–	3.1 400

^{a)}The signal intensities for the supercooled liquids and the aqueous solutions were not sufficient to perform lifetime and PLQY measurements. ^{b)}(–) Not possible to determine; ^{c)}Data obtained from TDFT calculations.

of the molten materials^[41] followed by fast cooling could be an alternative strategy to achieve thin films of higher quality. Alternatively, the SMs could be used as the minority guest in a blend with a majority (amorphous) host for the attainment of a uniform host-guest film. Such experiments are planned for our future research on the application of these and similar SMs.

2.5. Computational Study

As the observed electronic transitions occur within the cations only (albeit being perturbed by the surrounding), quantum-chemical calculations at the TDFT level were performed for the isolated cations in the gas phase (for details, see Experimental Section). In all cases, the S_1 excited state from which light emission occurs results from a HOMO-LUMO transition (Figure 5). Both HOMO and LUMO wave functions have π -type symmetry, and thus the S_1 state could be assigned to a π - π^* nature. Some comments can be made on the charge distribution and reorganization associated with the S_1 state: the LUMO of all cations shows that most of the electron density is located on the pyridine ring with reduced electron density on the phenolic fragment. In contrast, the HOMO shows that the electron density is located on the phenolic ring and less so on the pyridine ring. An introduction of a methyl group at the 2-position of [8HqH]⁺ (at the pyridine ring) raises the energy of the LUMO

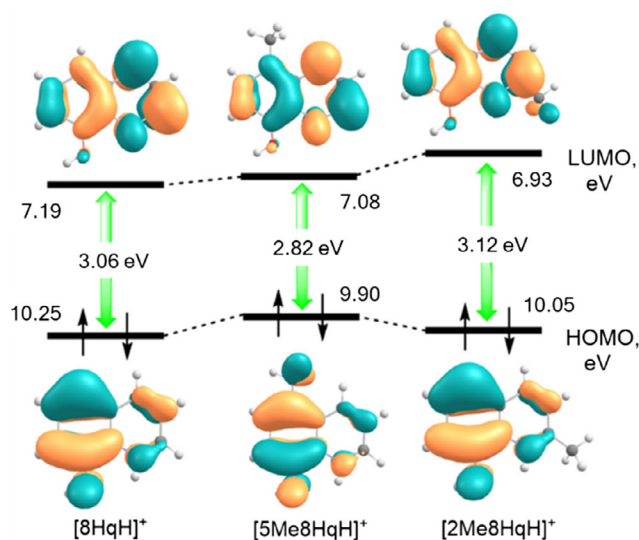


Figure 5. The shape and energy of frontier molecular orbitals for [8HqH]⁺, [5Me8HqH]⁺, and [2Me8HqH]⁺ calculated using B3LYP/6-31 + G(d,p) basis set at the S_1 state geometry.

but leaves the energy of the HOMO unperturbed to first order. The introduction of a methyl group to the 5-position of [8HqH]⁺ (at the phenolic ring) raises the HOMO and leaves the LUMO energy unperturbed in a first approximation. Consequently, a blue-shift of absorption is expected for [2Me8HqH]⁺, whilst for [5Me8HqH]⁺ a red shift when compared to [8HqH]⁺, which is confirmed by absorption spectroscopy (Figure 2). The calculated HOMO-LUMO gaps (Figure 5) match well with those determined from absorption spectroscopy (ΔE_{λ} in Table 2), being: 3.06 eV (1), 2.82 eV (2), and 3.12 eV (3), respectively. The charge reorganization during light emission and absorption makes the molecules also prone to solvatochromic effects. The HOMO has a strong contribution from the 2- p orbital of oxygen. Dissolution of the cation in water leads to an interaction of the phenolic group with water which stabilizes the HOMO, thus, widening the bandgap and leading to a blue shift in emission.

To explore the deactivation pathways of the S_1 state, the rate of intersystem crossing (k_{ISC}) between the S_1 state and the low-lying T_1 state (the only triplet state which is lying below the S_1 state) was calculated. Large S_1 - T_1 energy gaps (0.68, 0.61, and 0.69 eV for [8HqH]⁺, [5Me8HqH]⁺, and [2Me8HqH]⁺, respectively) and extremely small spin-orbit coupling (SOC) matrix elements between the S_1 and T_1 states (0.01 cm^{-1} for [8HqH]⁺, [2Me8HqH]⁺ cations, and only 0.001 cm^{-1} for [5Me8HqH]⁺) where calculated, which lead to remarkably low values of k_{ISC} ($1.1 \times 10^3 \text{ s}^{-1}$, $1.0 \times 10^3 \text{ s}^{-1}$, and $1.8 \times 10^1 \text{ s}^{-1}$). Therefore, ISC is slow and cannot quench the fluorescence emission. For that reason, S_1 - S_0 radiationless internal conversion (IC) should be the main radiationless deactivation channel for the S_1 state, either through fast proton exchange or vibronic coupling. Assuming that non-adiabatic coupling matrix elements (NACME) between S_1 and S_0 states for the related [8HqH]⁺, [5Me8HqH]⁺, and [2Me8HqH]⁺ cations are similar, the degree of IC should be proportional to the S_1 - S_0 energy gap (the smaller the gap the higher the k_{IC} rate). Indeed, from Table 2 it is possible

to see a clear correlation between fluorescence wavelength (460, 488, and 455 nm) and fluorescence QY (20%, 49%, and 13%) within the series of $[8\text{HqH}]^+$, $[5\text{Me}8\text{HqH}]^+$, and $[2\text{Me}8\text{HqH}]^+$ cations. Our calculations of the S_1 state radiative lifetime (298, 334, and 291 ns for $[8\text{HqH}]^+$, $[5\text{Me}8\text{HqH}]^+$, and $[2\text{Me}8\text{HqH}]^+$, respectively) are in a good qualitative agreement with experimentally observed values (200, 184, and 95 ns for $[8\text{HqH}]^+$, $[5\text{Me}8\text{HqH}]^+$, and $[2\text{Me}8\text{HqH}]^+$, respectively, estimated as τ/QY). The S_1 state is unusually long-lived as for common strong organic fluorophores the radiative lifetimes never exceed 10 ns.^[42]

2.6. Electrochemistry

To experimentally validate the HOMO and LUMO energy levels, the electrochemical redox behavior of **1–3** was investigated by cyclic voltammetry in acetonitrile solution (Table 4, Figure S31, Supporting Information). The electrochemical energy gaps calculated from the difference between the onset of oxidation (E_{ox}) and the onset of reduction (E_{red}) amount to: 3.34 eV (**1**), 3.07 eV (**2**), and 3.44 eV (**3**). The HOMO and LUMO energies were calculated from the measured redox peaks using Equation (2) taking into account that the redox energy of the Fc/Fc^+ couple is 4.8 eV with respect to the vacuum level^[43]

$$E_{\text{HOMO/LUMO}} = -(E_{\text{ox/red}} + 4.8)\text{eV} \quad (2)$$

Table 4. Electrochemical properties of **1–3**.^{a)}

	E_{red} [V] ^{b)}	E_{ox} [V] ^{b)}	HOMO [eV]	LUMO [eV]	ΔE [eV] ^{c)}	ΔE_{e} [eV] ^{d)}	ΔE_{g} [eV] ^{e)}
1	−1.36	1.97	−6.46	−3.13	3.34 (371 nm)	3.06 (405 nm)	3.06 (405 nm)
2	−1.34	1.72	−6.21	−3.15	3.07 (404 nm)	2.82 (440 nm)	2.84 (437 nm)
3	−1.45	1.99	−6.48	−3.04	3.44 (360 nm)	3.12 (397 nm)	3.12 (397 nm)

^{a)} 10^{-3} M acetonitrile solutions with 0.1 M LiTf_2N in N_2 -saturated acetonitrile at room temperature, potentials reported versus Fc/Fc^+ . ^{b)} $E_{\text{ox/red}}$ is the $E_{1/2}$ of the oxidation or reduction process obtained with a silver pseudo-reference electrode. ^{c)} HOMO–LUMO gap obtained from experimental data from cyclic voltammetry. ^{d)} HOMO–LUMO gap obtained from the DFT calculations. ^{e)} optical bandgap obtained from experimental data from absorption spectra.

The electrochemical HOMO and LUMO levels are shifted to higher energies compared to those derived by TDFT calculations and absorption spectra. Most likely, this blue shift originates from a solvatochromic effect. More specifically, a dissolution in acetonitrile (like in water) leads to a stabilization of the HOMO, and to a lesser extent the LUMO.

2.7. Electroluminescence

Electroluminescence of compounds **1–3** in solution was investigated with the aid of a high frequency (HF) Tesla generator. Figure 6 shows the blue emissions for **1** and **3** as well as the blue-green emission for **2**, in agreement with the observed photoluminescence. Since it was not possible to combine the electroluminescence experiment with the spectrofluorometer detector, it was not possible to record the spectra.

3. Conclusions

In this work, the 8-hydroxyquinolinium cation was identified as a lead structure for luminescent ionic small molecules. The compounds could be easily synthesized from commercial starting materials in a two-step synthetic procedure. The obtained compounds showed comparable, and in some cases even superior, photoluminescence relative to Alq_3 and related materials, both as solids and thin films. The structural rigidity, evoked by unique hydrogen bonding networks and π -stacking, aside from Coulombic interactions, leads to reduced mobility of the phenolic and pyridinium hydrogen atoms which appears to be key for the high luminescence QYs, hindering radiationless decay. Consequently, QYs between 40% and 50% could be reached. Modification of the HOMO–LUMO gap through substitution enabled a tuning of the emission color from deep blue (455 nm) to blue-green (488 nm). We believe that the efficient color-tunable ionic small molecule emitting materials with superior photoluminescence and high QY synthesized and characterized in this work show a lot of promise for further exploration in the field of light-emitting electrochemical devices.

4. Experimental Section

Synthesis of: 8-hydroxyquinolinium bis(trifluoromethanesulfonyl)imide (**1**), $[8\text{HqH}][\text{Tf}_2\text{N}]$, 5-methyl-8-hydroxyquinolinium bis(trifluoromethanesulfonyl)imide $[5\text{Me}8\text{HqH}][\text{Tf}_2\text{N}]$ (**2**), and >2-methyl-8-hydroxyquinolinium

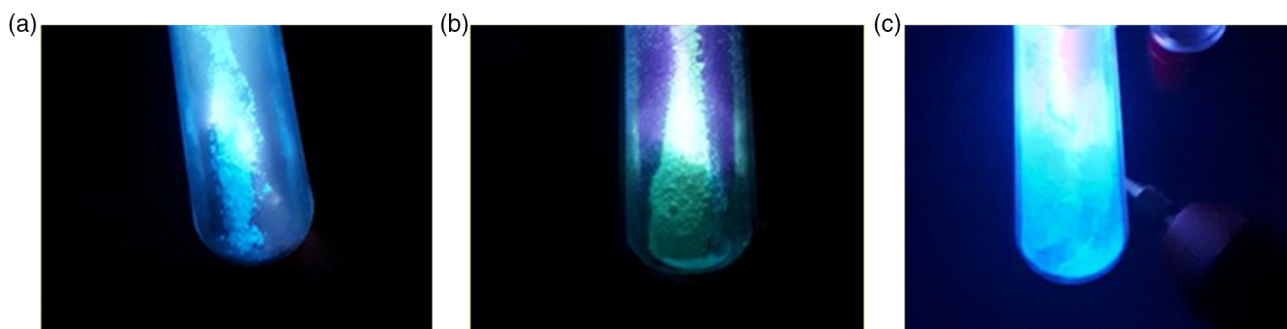


Figure 6. The blue and blue-green electroluminescence of: a) **1**, b) **2**, and c) **3** in a Schlenk flask under vacuum exposed to the HF Tesla generator.

bis(trifluoromethanesulfonyl)imide [2Me8HqH][Tf₂N] (**3**): All starting materials were purchased from Sigma Aldrich (Steinheim, Germany) and used without further purification. 8-Hydroxyquinoline (8Hq), 5-methyl-8-hydroxyquinoline (5Me8Hq), or 2-methyl-8-hydroxyquinoline (2Me8Hq) (10 mmol, 1 eq.) was dispersed in deionized water (20 mL). Dropwise addition of an aqueous solution of H₂SO₄ 98% (5 mmol, 0.5 eq., 10 mL) under cooling with an ice bath yielded yellow solutions. Solvent removal in the rotatory evaporator led to yellow solids ([8HqH]₂[SO₄], [5Me8HqH]₂[SO₄], [2Me8HqH]₂[SO₄]) with quantitative yield. Each sulfate salt (5 mmol, 1 eq.) was dissolved in deionized water (20 mL) mixed with bis(trifluoromethanesulfonyl)imide (LiTf₂N) (11.5 mmol, 2.3 eq.) dissolved in deionized water (20 mL). The mixing of the two solutions caused immediate turbidity that disappeared after stirring at room temperature overnight. The resulting solutions were then extracted with ethyl acetate and dried under vacuum to obtain brownish [8HqH][Tf₂N] (**1**), light yellow [5Me8HqH][Tf₂N] (**2**), or white [2Me8HqH][Tf₂N] (**3**) solids in a quantitative yield. 1) [8HqH][Tf₂N]: ¹H-NMR (400 MHz, DMSO-*d*₆, δ): 7.44 (dd, *J*_{H-H} = 5.2 Hz, *J*_{H-H} = 3.6 Hz, 1 H), 7.72–7.77 (m, 2 H), 8.02 (dd, *J*_{H-H} = 8.4 Hz, *J*_{H-H} = 5.6 Hz, 1 H), 9.06 (d, *J*_{H-H} = 6.4 Hz, 1 H), 9.08 (d, *J*_{H-H} = 9.2 Hz, 1 H), 11.89 (bs, 1 H). ¹³C-NMR (100 MHz, DMSO-*d*₆, δ): 115.7, 118.6, 119.6 (d, *J*_{C-F} = 320.0 Hz), 122.4, 129.5, 129.8, 130.3, 144.6, 145.8, 148.7. ¹⁹F-NMR (376 MHz, DMSO-*d*₆, δ): –79.20. ESI MS TOF: *m/z* (positive mode, {[8HqH]⁺}) 145.9907 (calculated *m/z* = 146.0600). FTIR: ν_{\max} (cm^{–1}) = 3239, 3214, 3184, 3094, 1637, 1605, 1595, 1556, 1519, 1501, 1476, 1424, 1403, 1375, 1356, 1338, 1307, 1291, 1239, 1230, 1185, 1129, 1097, 1036, 988, 910, 891, 817, 802, 787, 773, 761, 742, 659, 618, 594, 582, 569, 535, 506, 489, 466, 421, 403. 2) [5Me8HqH][Tf₂N]: ¹H-NMR (400 MHz, DMSO-*d*₆, δ): 2.66 (s, 3 H), 3.68 (bs, 1 H), 7.35 (d, *J*_{H-H} = 7.9 Hz, 1 H), 7.59 (dd, *J*_{H-H} = 0.8 Hz, *J*_{H-H} = 7.9 Hz, 1 H), 8.06 (dd, *J*_{H-H} = 5.2 Hz, *J*_{H-H} = 8.6 Hz, 1 H), 9.08 (dd, *J*_{H-H} = 1.3 Hz, *J*_{H-H} = 5.2 Hz, 1 H), 9.17 (dd, *J*_{H-H} = 1.3 Hz, *J*_{H-H} = 8.2 Hz, 1 H), 11.64 (bs, 1 H). ¹³C-NMR (100 MHz, DMSO-*d*₆, δ): 17.2, 115.4, 119.5 (d, *J*_{C-F} = 320.0 Hz), 121.9, 124.3, 125.6, 128.7, 130.1, 142.8, 143.9, 146.7. ¹⁹F-NMR (376 MHz, DMSO-*d*₆, δ): –78.74. ESI MS TOF: *m/z* (positive mode, {[5Me8HqH]⁺}) 160.0064 (calculated *m/z* = 160.0757). FTIR: ν_{\max} (cm^{–1}) = 3371, 3237, 3209, 3182, 3089, 1634, 1598, 1558, 1501, 1457, 1425, 1390, 1360, 1344, 1321, 1305, 1267, 1183, 1124, 1079, 1054, 967, 874, 836, 793, 767, 741, 698, 646, 593, 570, 530, 508, 452, 428, 402. 3) [2Me8HqH][Tf₂N]: ¹H-NMR (400 MHz, DMSO-*d*₆, δ): 2.97 (s, 3 H), 3.50 (bs, 1 H), 7.44 (dd, *J*_{H-H} = 3.7 Hz, *J*_{H-H} = 5.3 Hz, 1 H), 7.70 (d, *J*_{H-H} = 3.6 Hz, 1 H), 7.71 (d, *J*_{H-H} = 5.4 Hz, 1 H), 7.92 (d, *J*_{H-H} = 8.6 Hz, 1 H), 8.96 (d, *J*_{H-H} = 8.6 Hz, 1 H), 11.87 (bs, 1 H). ¹³C-NMR (100 MHz, DMSO-*d*₆, δ): 20.5, 116.1, 119.5 (d, *J*_{C-F} = 320.0 Hz), 118.6, 124.3, 128.0, 128.7, 129.5, 145.2, 147.8, 157.7. ¹⁹F-NMR (376 MHz, DMSO-*d*₆, δ): –78.73. ESI MS TOF: *m/z* (positive mode, {[2Me8HqH]⁺}) 160.0064 (calculated *m/z* = 160.0757). FTIR: ν_{\max} (cm^{–1}) = 3340, 3294, 3255, 3177, 314, 3112, 3093, 3066, 3013, 2933, 2816, 1949, 1792, 1748, 1646, 1606, 1545, 1513, 1474, 1421, 1392, 1367, 1339, 1317, 1305, 1227, 1189, 1126, 1055, 926, 897, 866, 848, 791, 755, 742, 696, 644, 592, 572, 534, 511, 496, 439, 422, 406.

Nuclear Magnetic Resonance Spectroscopy: ¹H- and ¹³C-nuclear magnetic resonance spectroscopy (NMR) spectra were recorded at room temperature in DMSO on a Bruker 400 MHz spectrometer equipped with a BBO probe (Karlsruhe, Germany). ¹⁹F-NMR were recorded at room temperature in DMSO on a Bruker 400 Ultrashield (Postdam, Germany). Chemical shifts are reported in delta (δ) units, expressed in parts per million (ppm). The following abbreviations are used for the observed multiplicities: s (singlet), d (doublet), dd (double doublet), bs (broad singlet), m (multiplet for unresolved lines). ¹H-NMR chemical shifts were referenced to the residual solvent signal for DMSO (2.50 ppm), and ¹³C-NMR chemical shifts were referenced to the solvent signal for DMSO (39.52 ppm).

Fourier Transformation Infrared Spectroscopy: Fourier transformation infrared spectroscopy (FTIR) spectra were collected with a Bruker Alpha-P ATR-spectrometer (Karlsruhe, Germany) in an attenuated total reflection configuration. The data evaluation was carried out with the program OPUS (Bruker, Karlsruhe, Germany).

ESI TOF Mass Spectrometry: An SYNAPT G2-S HDMS Q-ToF Mass Spectrometer (Waters, Manchester, UK) with an ESI operated in the positive and negative ion mode, was used in this study. The ion source was set up as follows: capillary voltage: 2500 V, extractor: 1.0 V, RF lens: 0.5 V, ion source temperature: 120 °C, and desolvation temperature 250 °C. Nitrogen was used as both the cone and desolvation gas at a flow of 70 and 500 L h^{–1}, respectively. Argon was used as collision gas at a pressure of 2.95 × 10^{–4} mbar. The data reported correspond to low-resolution mass spectrometry (LRMS).

Thermal Characterization: DSC was performed with a computer-controlled PhoenixDSC 204 F1 thermal analyzer (Netzsch, Selb, Germany). Measurements were carried out at a heating rate of 1 °C min^{–1} in a sealed aluminum crucible with an argon flow rate of 40 mL min^{–1}. The samples were placed in aluminum pans which were cold-sealed and punctured. Given temperatures correspond to the onsets of the respective thermal process.

TGA was performed with a TG 449 F3 Jupiter (Netzsch, Selb, Germany), using aluminum oxide crucibles with a heating rate of 10 °C min^{–1} and argon as a purge gas. Given temperatures correspond to the 5% onset of the respective thermal process.

Single Crystal X-ray Diffraction: Single-crystal X-ray diffraction (SCXRD) data of **1** and **3** were recorded using a Bruker D8 Venture (Mo K α , λ = 0.7093 Å at 293 K). SCXRD data of **2** were recorded using a Bruker D8 Venture (Cu K α , λ = 1.5406 Å at 293 K). The crystals of **2** were measured with Cu radiation due to bad crystallinity and, consequently, missing high-angle data. Data reduction was performed with the program package X-Red or SAINT and absorption corrections were carried out with the programs X-Shape or SADABS. Crystal structure solution was carried out using SHELXT^[44] within Olex2.^[45] Refinement was performed with SHELXL^[44]. Hydrogen atoms were added and treated with the riding atom mode. The hydrogens on the OH groups were fixed with regard to their orientation to the nearest electron acceptors. To illustrate the crystal structures, the program Diamond^[46] was used.

Powder X-ray Diffraction: Powder X-ray diffraction (PXRD) data of **1** and **3** were recorded at ambient temperature on a PANalytical X'pert PRO diffractometer (Malvern Panalytical, Malvern, UK), operating at 45 kV and 40 mA and using CuK α radiation (λ = 1.5406 Å at 293 K). The data was recorded in reflection mode from 5° to 70° with a rate of 0.55 sec/step. In the pattern obtained for **1**, a minor secondary phase (less than 1%) could be seen as a couple of broad peaks slightly above noise level (2θ = 15.8°, 17.6°) which did not match any of the starting materials. Also in the pattern obtained for **3** a minor secondary phase (less than 1%) could be seen as a single broad peak at noise level (2θ = 8.2°). Since samples of **2** could not be properly powdered resulting in strong preferred orientation and wrong peak intensities, a few big pieces were mounted on a wire and a 360° rotation scan has been executed at ambient temperature on a Bruker Venture diffractometer using MoK α (λ = 0.7093 Å at 293 K). The Debye rings have been integrated and converted with the APEX3 software (Bruker, 2016), resulting in the pattern presented in Figure S9, Supporting Information. The pattern confirmed the sample purity but it was not suitable for further refinement. The Rietveld refinements^[47] were performed for **1** and **3** with Fullprof Suite.^[48] Predicted PXRD diffractograms were calculated using Mercury.^[49]

Instrumentation: Absorption Spectroscopy: The UV–vis absorbance spectra were recorded on powder samples made from crystals of **1–3** and on 2 × 10^{–4} M aqueous solutions using an Agilent Technologies Cary 5000 UV–vis–NIR spectrophotometer equipped with an Agilent Praying Mantis diffuse reflectance accessory (Agilent Technologies, Kista, Sweden). A Spectralon disk was used as the reference material for the measurements on powder. Water was used as a reference for the solutions.

Photoluminescence: Steady-state fluorescence excitation, emission spectra, and fluorescence decay curves were recorded on a HORIBA Jobin Yvon FluoroLog-3 modular spectrofluorometer with an R928P PMT detector (Horiba France, Longjumeau, France). A 450 W xenon arc lamp was used for the steady-state measurements, whereas a Fianium WhiteLase super-continuum laser (NKT Photonics, Birkerød, Denmark) with the instrument operating in a TCPS mode was used for lifetime measurements. Quantum

yields (QYs) were determined with an integrating sphere using BaSO₄ as a reference.

Computational Study: The molecular structure of the [8HqH]⁺, [2Me8HqH]⁺, and [5Me8HqH]⁺ cations were initially optimized using the DFT/B3LYP/6-31 + G(d,p) method^[50] in their singlet ground (S₀) electronic state. Based on the obtained S₀ state structures, the first singlet (S₁) and first triplet (T₁) excited state geometries were optimized using TDDFT/B3LYP/6-31 + G(d,p) and UB3LYP/6-31 + G(d,p) methods,^[50] respectively. Grimme's empirical dispersion correction (GD3)^[51] was additionally used in all optimization procedures.

Based on the S₁ state geometries SOC effects were treated as a perturbation based on the scalar relativistic (SR) orbitals after self-consistent field (SCF) and TDFT calculations (pSOC-TDDFT);^[52] B3LYP functional and Slater-type TZP all-electron basis sets^[53] were used for these calculations. The SOC matrix elements, (only the T₁ state has smaller energy than S₁ state) were calculated as the root mean squares, i.e., as the square root of the sum of squares of SOC matrix elements of all triplet state sublevels ($m = 0 \pm 1$) of the uncoupled states, as presented in Equation (3).^[54]

$$\langle S_1 | \hat{H}_{SO} | T_1 \rangle = \sqrt{\sum_{m=0,\pm 1} \langle S_1 | \hat{H}_{SO} | T_1^m \rangle^2} \quad (3)$$

The SOC coupling operator \hat{H}_{SO} was considered in our calculations within the zeroth-order regular approximation (ZORA)^[55] in accordance with Equation (4).

$$\hat{H}_{SO} = \frac{c^2}{(2c^2 - V)} \sigma(\nabla V \cdot \mathbf{p}) \quad (4)$$

where σ is the Pauli spin matrix vector, \mathbf{p} is the linear momentum operator, c is the speed of light, and V is the Kohn–Sham potential. The fluorescence rate constants (k_r) were estimated according to Equation (5) (expressed in atomic units).^[56]

$$k_r = \frac{1}{\tau} = \frac{2(\Delta E)^2 f}{c^3} \quad (5)$$

where τ is the electric dipole radiative life of the S₁ state while ΔE and f are the energy and intensity of the corresponding S₁ → S₀ transition accounting for SOC perturbations.

The pSOC-TDDFT calculations were carried out using the ADF2019 package^[57] while the remaining calculations were performed using the Gaussian16 software.^[58]

The rate constants of intersystem crossing (ISC) between the S₁ and T₁ states were estimated using the Plotnikov's simple empirical approximation with Equation (6)^[59]

$$k_{S_1 \rightarrow T_1} = 10^{10} \langle S_1 | \hat{H}_{SO} | T_1 \rangle^2 F_{0m} \quad (6)$$

where Franck–Condon factors (F_{0m}) were approximated using Equation (7)

$$F_{0m} = \sum_n \prod_v \frac{e^{-\gamma} \gamma^{n_v}}{n_v!} \quad (7)$$

In Equation (6) the Huang–Rhys factor γ was assumed to be equal to 0.3 and only one average promotive mode $\omega_v = 1400 \text{ cm}^{-1}$ was used when considering $n_v = \Delta E(S_1 - T_1) / \omega_v$. Such a single-mode approximation was considered efficient and accurate enough for the organic dyes and fluorophores.^[60]

Electrochemistry: Cyclic voltammetry analysis was conducted on a Gamry Instrument Interface 1010 potentiostat (Warminster, Pennsylvania, United States) via the three electrodes method.^[61] Glassy carbon ($d = 3 \text{ mm}$) was used as a working electrode, Pt coil as a counter electrode, and a capillary with septum containing an Ag rod submerged in a solution 0.1 M LiTf₂N in N₂-saturated acetonitrile as a reference electrode. Multiple scans were conducted at 100 mV s^{−1} on a 10^{−3} M solution

of: 1) [8HqH][Tf₂N], 2) [5Me8HqH][Tf₂N], and 3) [2Me8HqH][Tf₂N] in acetonitrile. LiTf₂N was used as the additional electrolyte.

[CCDCs 1963 861, 2 041 903, 2 041 904 contains the supplementary crystallographic data for this article. These data can be obtained free of charge from The Cambridge Crystallographic Data Centre via www.ccdc.cam.ac.uk/data_request/cif.]

Supporting Information

Supporting Information is available from the Wiley Online Library or from the author.

Acknowledgements

The Swedish Research Council is acknowledged for a Tage Erlander Professorship to Robin D. Rogers, the Royal Academy of Science for the support through the Göran Gustafsson prize in Chemistry to Anja-Verena Mudring, the Swedish Energy Agency for support through project no. 46676-1 (Anja-Verena Mudring) and no. 50779-1 (Ludvig Edman), Swedish Research Council (starting grant no. 2020-04600, Glib V. Baryshnikov, project grant no. 2021-04778, Ludvig Edman), and the Swedish Foundation for Strategic Research (project EM16-0013, Ludvig Edman). Anja-Verena Mudring acknowledges support to Guillaume Bousrez within the SSF-funded REFIT project and to VR project no. 2020-04437. The quantum-chemical calculations were performed with computational resources provided by Swedish National Infrastructure for Computing (SNIC 2021-3-22) at the High-Performance Computing Center North (HPC2N) partially funded by the Swedish Research Council through the grant agreement no. 2018-05973. The authors would like to thank Dr. Mark Nieuwenhuyzen for his contribution to the elucidation of the crystal structure of: 1) [8HqH][Tf₂N].

Conflict of Interest

The authors declare no conflict of interest.

Data Availability Statement

The data that support the findings of this study are available from the corresponding author upon reasonable request.

Keywords

crystal engineering, organic lighting, photoluminescence, secondary bonding interactions

Received: October 11, 2022

Revised: November 26, 2022

Published online: February 3, 2023

- [1] G. Dreyfus, C. Gallinat, <https://www.energy.gov/articles/rise-and-shine-lighting-world-10-billion-led-bulbs> (accessed: January 2023).
- [2] IEA (2020), <https://www.iea.org/reports/world-energy-outlook-2020/outlook-for-electricity#abstract> (accessed: March 2021).
- [3] A. Salehi, X. Fu, D.-H. Shin, F. So, *Adv. Funct. Mater.* **2019**, 29, 1808803.
- [4] a) E. Fresta, R. D. Costa, *J. Mater. Chem. C* **2017**, 5, 5643; b) A. Sandström, L. Edman, *Energy Technol.* **2015**, 3, 329.
- [5] A. Sandström, H. F. Dam, F. C. Krebs, L. Edman, *Nat. Commun.* **2012**, 3, 1002.

- [6] M. H. Bowler, A. Mishra, A. C. Adams, C. L. D. Blangy, J. D. Slinker, *Adv. Funct. Mater.* **2020**, *30*, 1906715.
- [7] A. Asadpoordarvish, A. Sandström, S. Tang, J. Granström, L. Edman, *Appl. Phys. Lett.* **2012**, *100*, 193508.
- [8] a) A. M. Bünzli, E. C. Constable, C. E. Housecroft, A. Prescimone, J. A. Zampese, G. Longo, L. Gil-Escrig, A. Pertegás, E. Ortí, H. J. Bolink, *Chem. Sci.* **2015**, *6*, 2843; b) J. Mindemark, S. Tang, J. Wang, N. Kaihovirta, D. Brandell, L. Edman, *Chem. Mater.* **2016**, *28*, 2618.
- [9] a) D. Ma, T. Tsuboi, Y. Qiu, L. Duan, *Adv. Mater.* **2017**, *29*, 1603253; b) M. Martínez-Alonso, J. Cerdá, C. Momblona, A. Pertegás, J. M. Junquera-Hernández, A. Heras, A. M. Rodríguez, G. Espino, H. Bolink, E. Ortí, *Inorg. Chem.* **2017**, *56*, 10298; c) S. Karimi, H. Shahroosvand, S. Bellani, F. Bonaccorso, *J. Phys. Chem. C* **2021**, *125*, 819; d) L. M. Cavinato, S. Wölfl, A. Pöthig, E. Fresta, C. Garino, J. Fernandez-Cestau, C. Barolo, R. D. Costa, *Adv. Mater.* **2022**, *34*, 2109228.
- [10] a) W. K. Bae, J. Lim, D. Lee, M. Park, H. Lee, J. Kwak, K. Char, C. Lee, S. Lee, *Adv. Mater.* **2014**, *26*, 6387; b) H. Jia, Z. Wang, T. Yuan, F. Yuan, X. Li, Y. Li, Z. A. Tan, L. Fan, S. Yang, *Adv. Sci.* **2019**, *6*, 1900397; c) Y.-H. Won, O. Cho, T. Kim, D.-Y. Chung, T. Kim, H. Chung, H. Jang, J. Lee, D. Kim, E. Jang, *Nature* **2019**, *575*, 634; d) H. Moon, W. Lee, J. Kim, D. Lee, S. Cha, S. Shin, H. Chae, *Chem. Commun.* **2019**, *55*, 13299; e) C.-Y. Han, S.-H. Lee, S.-W. Song, S.-Y. Yoon, J.-H. Jo, D.-Y. Jo, H.-M. Kim, B.-J. Lee, H.-S. Kim, H. Yang, *ACS Energy Lett.* **2020**, *5*, 1568; f) S.-Y. Yoon, Y.-H. Kim, D.-Y. Jo, J.-H. Jo, S.-H. Lee, H.-M. Kim, Y. Kim, S.-K. Kim, H. Yang, *Chem. Eng. J.* **2021**, *410*, 128426.
- [11] a) J. Choi, S. Kanagaraj, Y. Choe, *J. Mater. Chem. C* **2020**, *8*, 4580; b) T. Zhang, R. Xu, H. Lv, Z. Wang, H. Ye, H. Liu, L. Chen, *Optik* **2022**, *261*, 169176; c) H.-L. Shen, P.-W. Hsiao, R.-H. Yi, Y.-H. Su, Y. Chen, C.-W. Lu, H.-C. Su, *Dyes Pigm.* **2022**, *203*, 110346; d) A. Puthanveedu, K. Shanmugasundaram, S. Yoon, Y. Choe, *J. Mater. Chem. C* **2022**, *10*, 2245.
- [12] M. S. Subeesh, K. Shanmugasundaram, C. D. Sunesh, Y. S. Won, Y. Choe, *J. Mater. Chem. C* **2015**, *3*, 4683.
- [13] H.-F. Chen, C.-T. Liao, T.-C. Chen, H.-C. Su, K.-T. Wong, T.-F. Guo, *J. Mater. Chem.* **2011**, *21*, 4175.
- [14] a) C.-T. Liao, H.-F. Chen, H.-C. Su, K.-T. Wong, *J. Mater. Chem.* **2011**, *21*, 17855; b) J.-S. Lu, H.-F. Chen, J.-C. Kuo, R. Sun, C.-Y. Cheng, Y.-S. Yeh, H.-C. Su, K.-T. Wong, *J. Mater. Chem. C* **2015**, *3*, 2802.
- [15] a) M. S. Subeesh, K. Shanmugasundaram, C. D. Sunesh, T. P. Nguyen, Y. Choe, *J. Phys. Chem. C* **2015**, *119*, 23676; b) M. Y. Wong, M.-G. La-Placa, A. Pertegas, H. J. Bolink, E. Zysman-Colman, *J. Mater. Chem. C* **2017**, *5*, 1699.
- [16] a) M. J. Jafari, J. Liu, I. Engquist, T. Ederth, *ACS Appl. Mater. Interfaces* **2017**, *9*, 2747; b) K.-Y. Lin, L. D. Bastatas, K. J. Suhr, M. D. Moore, B. J. Holliday, M. Minary-Jolandan, J. D. Slinker, *ACS Appl. Mater. Interfaces* **2016**, *8*, 16776; c) L. D. Bastatas, K.-Y. Lin, M. D. Moore, K. J. Suhr, M. H. Bowler, Y. Shen, B. J. Holliday, J. D. Slinker, *Langmuir* **2016**, *32*, 9468; d) H.-F. Chen, C.-T. Liao, H.-C. Su, Y.-S. Yeh, K.-T. Wong, *J. Mater. Chem. C* **2013**, *1*, 4647.
- [17] a) M. Cölle, R. E. Dinnebie, W. Brütting, *Chem. Commun.* **2002**, *23*, 2908; b) J. Kido, Y. Izumi, *Chem. Lett.* **1997**, *26*, 963; c) S. So, K. Lee, W. Choi, L. Leung, W. Lo, *Jpn. J. Appl. Phys.* **2001**, *40*, 5959; d) P. Kumar, A. Misra, R. Bhardwaj, M. N. Kamalasanan, S. C. Jain, S. Chand, R. P. Tandon, *Displays* **2008**, *29*, 351.
- [18] C. W. Tang, S. A. VanSlyke, *Appl. Phys. Lett.* **1987**, *51*, 913.
- [19] R. Pohl, P. Anzenbacher, *Org. Lett.* **2003**, *5*, 2769.
- [20] A. Curioni, M. Boero, W. Andreoni, *Chem. Phys. Lett.* **1998**, *294*, 263.
- [21] a) S.-Y. Park, P. Ghosh, S. O. Park, Y. M. Lee, S. K. Kwak, O.-H. Kwon, *RSC Adv.* **2016**, *6*, 9812; b) S. G. Schulman, *Anal. Chem.* **1971**, *43*, 285.
- [22] M. Goldman, E. L. Wehry, *Anal. Chem.* **1970**, *42*, 1178.
- [23] R. E. Ballard, J. W. Edwards, *J. Chem. Soc.* **1964**, 4868.
- [24] a) R. Thirumurugan, B. Babu, K. Anitha, J. Chandrasekaran, *Spectrochim. Acta, Part A* **2015**, *140*, 44; b) S. Goel, H. Yadav, N. Sinha, B. Singh, I. Bdkin, B. Kumar, *Acta Crystallogr., Sect. B* **2018**, *74*, 12.
- [25] a) P. Bonhôte, A.-P. Dias, N. Papageorgiou, K. Kalyanasundaram, M. Grätzel, *Inorg. Chem.* **1996**, *35*, 1168; b) J. Sun, M. Forsyth, D. R. MacFarlane, *J. Phys. Chem. B* **1998**, *102*, 8858; c) J. S. Yadav, B. V. S. Reddy, C. S. Reddy, K. Rajasekhara, *J. Org. Chem.* **2003**, *68*, 2525; d) S. F. Lux, L. Terborg, O. Hachmöller, T. Placke, H. W. Meyer, S. Passerini, M. Winter, S. Nowak, *J. Electrochem. Soc.* **2013**, *160*, A1694; e) S. Zhang, J. Wang, X. Lu, Q. Zhou, in *Structures and Interactions of Ionic Liquids*, Vol. 151, Springer, Berlin **2013**.
- [26] a) I. V. Fedyanin, V. A. Karnoukhova, K. A. Lyssenko, *CrystEngComm* **2018**, *20*, 652–660; b) G. Malecki, J. E. Nycz, E. Ryrych, L. Ponikiewski, M. Nowak, J. Kusz, J. Pikies, *J. Mol. Struct.* **2010**, *969*, 130; c) J. E. Nycz, M. Szala, G. J. Malecki, M. Nowak, J. Kusz, *Spectrochim. Acta, Part A* **2014**, *117*, 351.
- [27] A. V. Mudring, A. Babai, S. Arenz, R. Giernoth, *Angew. Chem., Int. Ed.* **2005**, *44*, 5485.
- [28] a) P. Roychowdhury, B. N. Das, B. S. Basak, *Acta Crystallogr., Sect. B* **1978**, *34*, 1047–1048; b) T. Banerjee, N. N. Saha, *Acta Crystallogr., Sect. C* **1986**, *42*, 1408.
- [29] T. Steiner, *Angew. Chem., Int. Ed.* **2002**, *41*, 48.
- [30] A.-V. Mudring, *Aust. J. Chem.* **2010**, *63*, 544.
- [31] S. L. Srivastava, M. Prasad, . Rohitashava, *Spectrochim. Acta, Part A* **1984**, *40*, 681.
- [32] E. T. Spielberg, P. S. Campbell, K. C. Szeto, B. Mallick, J. Schaumann, A.-V. Mudring, *Chem. Eur. J.* **2018**, *24*, 15638.
- [33] Y. Ikabata, Q. Wang, T. Yoshikawa, A. Ueda, T. Murata, K. Kariyazono, M. Moriguchi, H. Okamoto, Y. Morita, H. Nakai, *npj Quantum Mater.* **2017**, *2*, 27.
- [34] a) O. Popovych, L. B. Rogers, *Spectrochim. Acta* **1959**, *15*, 584; b) S. Schulman, Q. Fernando, *Tetrahedron* **1968**, *24*, 1777; c) M. P. Bratzel, J. J. Aaron, J. D. Winefordner, S. G. Schulman, H. Gershon, *Anal. Chem.* **1972**, *44*, 1240.
- [35] H. S. Fairman, M. H. Brill, H. Hemmendinger, *Color Res. Appl.* **1997**, *22*, 11.
- [36] V. Balzani, P. Ceroni, A. Juris, *Photochemistry and Pphotophysics: Concepts, Research, Applications*, Wiley-VCH, Weinheim, Germany **2014**.
- [37] T. Tsuboi, Y. Torii, *Mol. Cryst. Liq. Cryst.* **2010**, *529*, 42.
- [38] S. Wu, X. Zhong, H. Zeng, W. You, W. Zhou, *J. Lumin.* **2018**, *195*, 120.
- [39] J. Tan, X. Li, Y. Zhan, J. Xiong, X. Lv, C. Pan, Y. Huo, *Polyhedron* **2018**, *155*, 398.
- [40] D. Z. Garbuzov, V. Bulović, P. E. Burrows, S. R. Forrest, *Chem. Phys. Lett.* **1996**, *249*, 433.
- [41] R. Dobužinskas, A. Poškus, M. Viliūnas, V. Jankauskas, M. Daškevičienė, V. Getautis, K. Arlauskas, *Phys. Status Solidi A* **2019**, *216*, 1900635.
- [42] M. Y. Berezin, S. Achilefu, *Chem. Rev.* **2010**, *110*, 2641.
- [43] a) T. Guo, L. Yu, B. Zhao, L. Ying, H. Wu, W. Yang, Y. Cao, *J. Polym. Sci., Part A: Polym. Chem.* **2015**, *53*, 1043–1051; b) S. Zhao, J. Liang, T. Guo, Y. Wang, X. Chen, D. Fu, J. Xiong, L. Ying, W. Yang, J. Peng, Y. Cao, *Org. Electron.* **2016**, *38*, 130.
- [44] G. Sheldrick, *Acta Crystallogr. Sect. A* **2015**, *71*, 3.
- [45] O. V. Dolomanov, L. J. Bourhis, R. J. Gildea, J. A. K. Howard, H. Puschmann, *J. Appl. Crystallogr.* **2009**, *42*, 339.
- [46] K. Brandenburg, H. Putz, Diamond, Crystal Impact **2011**.
- [47] H. Rietveld, *J. Appl. Crystallogr.* **1969**, *2*, 65.
- [48] J. Rodríguez-Carvajal, in *Abstracts of the Satellite Meeting on Powder Diffraction of the XV Congress of the IUCr*, Toulouse, France **1990**, p. 127.

- [49] C. F. Macrae, I. Sovago, S. J. Cottrell, P. T. A. Galek, P. McCabe, E. Pidcock, M. Platings, G. P. Shields, J. S. Stevens, M. Towler, P. A. Wood, *J. Appl. Crystallogr.* **2020**, 53, 226.
- [50] a) A. D. Becke, *J. Chem. Phys.* **1993**, 98, 5648–5652; b) C. Lee, W. Yang, R. G. Parr, *Phys. Rev. B* **1988**, 37, 785; c) R. Ditchfield, W. J. Hehre, J. A. Pople, *J. Chem. Phys.* **1971**, 54, 724; d) T. Clark, J. Chandrasekhar, G. W. Spitznagel, P. V. R. Schleyer, *J. Comput. Chem.* **1983**, 4, 294; e) M. J. Frisch, J. A. Pople, J. S. Binkley, *J. Chem. Phys.* **1984**, 80, 3265.
- [51] S. Grimme, J. Antony, S. Ehrlich, H. Krieg, *J. Chem. Phys.* **2010**, 132, 154104.
- [52] F. Wang, T. Ziegler, *J. Chem. Phys.* **2005**, 123, 154102.
- [53] E. Van Lenthe, E. J. Baerends, *J. Comput. Chem.* **2003**, 24, 1142.
- [54] P. K. Samanta, D. Kim, V. Coropceanu, J.-L. Brédas, *J. Am. Chem. Soc.* **2017**, 139, 4042.
- [55] a) E. van Lenthe, R. van Leeuwen, E. J. Baerends, J. G. Snijders, *Int. J. Quantum Chem.* **1996**, 57, 281; b) E. van Lenthe, J. G. Snijders, E. J. Baerends, *J. Chem. Phys.* **1996**, 105, 6505.
- [56] a) K. Mori, T. P. M. Goumans, E. van Lenthe, F. Wang, *PCCP* **2014**, 16, 14523; b) G. Baryshnikov, B. Minaev, H. Ågren, *Chem. Rev.* **2017**, 117, 6500.
- [57] G. te Velde, F. M. Bickelhaupt, E. J. Baerends, C. Fonseca Guerra, S. J. A. van Gisbergen, J. G. Snijders, T. Ziegler, *J. Comput. Chem.* **2001**, 22, 931.
- [58] M. J. Frisch, G. W. Trucks, H. B. Schlegel, G. E. Scuseria, M. A. Robb, J. R. Cheeseman, G. Scalmani, V. Barone, G. A. Petersson, H. Nakatsuji, X. Li, M. Caricato, A. V. Marenich, J. Bloino, B. G. Janesko, R. Gomperts, B. Mennucci, H. P. Hratchian, J. V. Ortiz, A. F. Izmaylov, J. L. Sonnenberg, D. Williams-Young, F. Ding, F. Lipparini, F. Egidi, J. Goings, B. Peng, A. Petrone, T. Henderson, D. Ranasinghe, et al, Gaussian, Inc., Wallingford, CT **2016**.
- [59] V. Plotnikov, *Int. J. Quantum Chem.* **1979**, 16, 527.
- [60] a) G. V. Baryshnikov, R. R. Valiev, N. N. Karaush, V. A. Minaeva, A. N. Sinelnikov, S. K. Pedersen, M. Pittelkow, B. F. Minaev, H. Ågren, *PCCP* **2016**, 18, 28040; b) R. R. Valiev, V. N. Cherepanov, V. Y. Artyukhov, D. Sundholm, *PCCP* **2012**, 14, 11508; c) V. Y. Artyukhov, T. Kopylova, L. Samsonova, N. Selivanov, V. Plotnikov, V. Sazhnikov, A. Khlebunov, G. Mayer, M. Alfimov, *Russ. Phys. J.* **2008**, 51, 1097; d) R. Valiev, A. Sinelnikov, Y. V. Aksenova, *Spectrochim. Acta* **2014**, 117, 323.
- [61] N. Elgrishi, K. J. Rountree, B. D. McCarthy, E. S. Rountree, T. T. Eisenhart, J. L. Dempsey, *J. Chem. Educ.* **2018**, 95, 197.